J. Fluid Mech. (1990), *vol.* 211, *pp.* 285–307
Printed in Great Britain

A supersonic turbulent boundary layer in an adverse pressure gradient

By EMERICK M. FERNANDO AND ALEXANDER J. SMITS
Department of Mechanical and Aerospace Engineering, Princeton University, Princeton, NJ 08544 USA

(Received 22 September 1988 and in revised form 12 July 1989)

This investigation describes the effects of an adverse pressure gradient on a flat plate supersonic turbulent boundary layer ($M_{\mathrm{ref}} \approx 2.9$, $\beta_{\max} \approx 5.8$, $Re_{\theta,\mathrm{ref}} \approx 75600$). Single normal hot wires and crossed wires were used to study the Reynolds stress behaviour, and the features of the large-scale structures in the boundary layer were investigated by measuring space–time correlations in the normal and spanwise directions. Both the mean flow and the turbulence were strongly affected by the pressure gradient. However, the turbulent stress ratios showed much less variation than the stresses, and the essential nature of the large-scale structures was unaffected by the pressure gradient. The wall pressure distribution in the current experiment was designed to match the pressure distribution on a previously studied curved-wall model where streamline curvature acted in combination with bulk compression. The addition of streamline curvature affects the turbulence strongly, although its influence on the mean velocity field is less pronounced and the modifications to the skin-friction distribution seem to follow the empirical correlations developed by Bradshaw (1974) reasonably well.

1. Introduction

The behaviour of a supersonic turbulent boundary layer in an adverse pressure gradient is of great practical interest to designers of turbo-machinery and high-speed aircraft. Previous investigations of such flows have dealt mostly with the mean flow behaviour, and only a few have reported turbulence measurements. These experiments indicate that the compression associated with an adverse pressure gradient in a supersonic flow strongly affects the turbulence behaviour, although the mechanism is not well understood. Bulk compression ($-\boldsymbol{\nabla}\cdot\boldsymbol{U}$) is an example of what Bradshaw (1973) terms an 'extra strain rate', that is, a strain rate additional to the simple shear $\partial U/\partial y$, and even small levels of extra strain rate, of the order of 0.01 $\partial U/\partial y$, have been found to have a significant effect on boundary-layer behaviour and turbulence. In the present study, extensive turbulence measurements were made in a flat-plate boundary layer with an externally imposed adverse pressure gradient to help understand the overall boundary-layer response, and to provide data to help develop and test new turbulence models.

Arguments based on the conservation of angular momentum can be used to show that bulk compression, concave curvature, and lateral divergence are examples of destabilizing extra strain rates. For example, Green (Bradshaw 1974) notes that lateral divergence and bulk compression both decrease the cross-sectional area of a fluid element in the (x, y)-plane, and by conservation of angular momentum tend to increase the spanwise component of vorticity. Similar arguments can be used to show

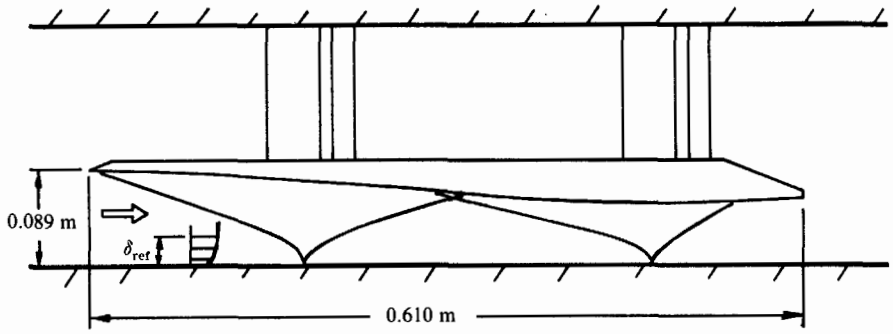

FIGURE 1. Schematic showing the relative positioning of the contoured plate in the test section, and the reflected wave system generated by it.

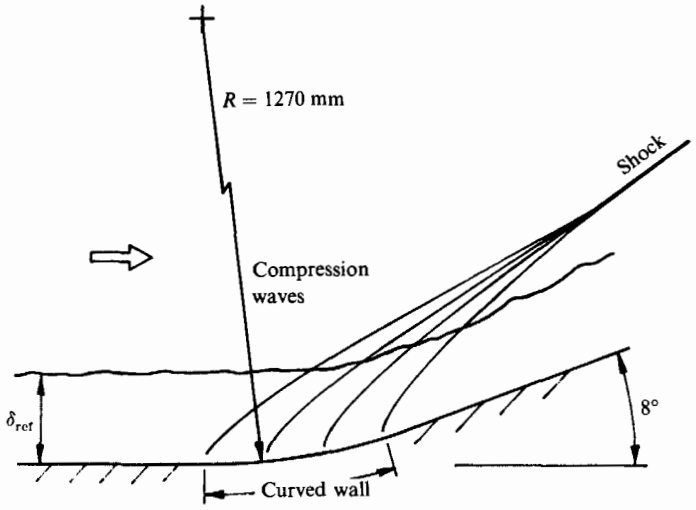

FIGURE 2. Circular arc Model II (Taylor 1984).

that the extra strain rates associated with dilatation, convex curvature, and lateral convergence are stabilizing in that they tend to reduce turbulent mixing.

The response of the boundary layer to combinations of extra strain rates, or to stabilizing and destabilizing versions of the same strain rate, appears to be quite nonlinear. For instance, the different response times and fundamentally different behaviour of boundary layers under the influence of concave or convex streamline curvature is well documented (Ramaprian & Shivaprasad 1978; Muck, Hoffman & Bradshaw 1985; and Hoffman, Muck & Bradshaw 1985). To take another example, Smits & Joubert (1982) demonstrated that the destabilizing influence of lateral streamline divergence, when combined with the stabilizing effect of convex curvature, results in a strongly stabilizing effect that is greater than that due to convex curvature alone.

In the present study, the adverse pressure gradient was imposed on the wall boundary layer by a wave generator mounted in the free stream (see figure 1). When the pressure gradient is generated in this way, streamline curvature effects are small. However. adverse pressure gradient flows are often generated by using concave surface curvature, and then the effects of adverse pressure gradient, bulk compression and concave streamline curvature all act simultaneously. Taylor (1984) studied a

number of flows with concave surface curvature, and to help differentiate between the effects of streamline curvature and bulk compression in one particular case the pressure distribution on the flat plate was designed so that it matched the pressure distribution for her Model II (figure 2). The flow over Model II has also been investigated extensively by Jayaram, Taylor & Smits (1987) and Donovan & Smits (1987) to determine the behaviour of the Reynolds stresses and the change in the large-scale structure of the boundary layer, and therefore it provides a useful companion experiment to the present flat-plate study.

2. Experimental apparatus

The experiments were carried out in the Princeton University 203 mm × 203 mm supersonic blowdown wind tunnel. The test boundary layer was the tunnel floor boundary layer, which was naturally turbulent without the use of any tripping devices. The tunnel stagnation conditions, and the flow conditions just upstream of the pressure gradient, are summarized in table 1.

To generate the adverse pressure gradient, a contoured plate was mounted in the free stream of the tunnel. The plate spanned the entire width of the tunnel, and it was held in place by two struts bolted to the tunnel ceiling (see figure 1). The boundary layer on the tunnel floor therefore experienced an adverse pressure gradient of the reflected-wave type. The pressure rose by a factor of approximately two in a distance equal to about $11\delta_{\mathrm{ref}}$, where δ_{ref} was the upstream boundary-layer thickness (see figure 3). The Mach number decreased from 2.9 to 2.5 in the same distance.

Standard techniques were used to determine the mean flow behaviour. Static pressures were measured with a cone-cylinder static pressure probe and Pitot pressures were measured using a flattened Pitot probe. The total temperature was determined using an unshielded thermocouple probe, and a Preston probe was used to obtain skin-friction data. Further details of these probes are given by Fernando (1988).

For the turbulence measurements, DANTEC 55M Series constant-temperature anemometers with the M12 symmetrical bridge were used. The hot-wire probes, including single normal-wire probes, dual normal-wire probes, and crossed-wire probes were custom-built. The probe prongs were made of stainless steel needles mounted in a cylindrical ceramic plug, which itself was held rigidly by a stainless steel probe holder. To minimize aerodynamic interference effects, a wedge-shaped epoxy nose was formed on the front of the ceramic plug. A 5 μm diameter tungsten wire, copper plated to 100 μm diameter was soft soldered to the tips of the prongs. The central portion of this wire was then etched to expose an active length of tungsten wire about 0.8 mm long, supported on either side by a copper plated stub. Experiments using stubs of 50 μm and 100 μm diameter showed that the 100 μm reduced wire breakage without affecting the turbulence measurements, and therefore the larger diameter stubs were used throughout.

The spanwise spacing between the two inclined wires of the crossed-wire probe was fixed at 1.2 mm to avoid aerodynamic interference effects due to the shock system generated by the wires and their supports (Fernando, Donovan & Smits 1987). This relatively large spacing limited the spatial resolution of the crossed-wire probe, significantly affecting the measurements near the wall. Mach number effects are also important, and the measurements are reliable only when the Mach number normal to each wire is supersonic (Smits & Muck 1984). It was found that Mach number effects and spatial resolution limits caused the crossed wire to underpredict the

Re_{ref}/m	6.3×10^7/m
$M_{e,ref}$	2.92
$p_{w,ref}$	2.1×10^2 N/m^2
p_0	6×10^5 N/m^2
T_0	270 K
T_w/T_0	1.04
$U_{e,ref}$	575 m/s
$\rho_{e,ref}$	0.75 kg/m^3
δ_{ref}	26.4 mm
δ^*_{ref}	7.2 mm
θ_{ref}	1.2 mm

TABLE 1. Nominal incoming flow conditions and tunnel stagnation conditions

Reynolds stresses for $y/\delta < 0.2$ in the upstream boundary layer ($x = 1.000$ m measured from the nozzle exit plane), and for $y/\delta < 0.46$ at $x = 1.254$ m, and $y/\delta < 0.42$ at 1.381 m, and the cross-wire results in these regions must be treated with caution (see solid symbols in figures 8–10).

The hot wires were operated in the constant-temperature mode at a high overheat ratio (≈ 1.0), so that the output was predominantly sensitive to fluctuations in mass flux and the 'contamination' due to total temperature fluctuations was small (Smits, Hayakawa & Muck 1983). The frequency response, as determined by a square-wave test, exceeded 200 kHz for all tests. In the upstream boundary layer, the total uncertainty in $\overline{(\rho u)'^2}$, $\overline{v'^2}$ and $-\overline{(\rho u)'v'}$ was estimated to be $\pm 15\%$, -21% to $+18\%$, and -22% to 12%, respectively. To estimate the streamwise velocity fluctuation intensity, the 'Strong Reynolds Analogy' was assumed to hold, so that

$$(\overline{\rho'^2})^{\frac{1}{2}}/\bar{\rho} = (\gamma - 1)M^2(\overline{u'^2})^{\frac{1}{2}}/\bar{U} \quad \text{and} \quad \overline{\rho'u'}/(\overline{\rho'^2})^{\frac{1}{2}}(\overline{u'})^{\frac{1}{2}} = 0.8$$

(see Spina & Smits 1987 for further details). With this assumption, the total uncertainty in $\overline{u'^2}$ and $-\overline{u'v'}$ was estimated to be $\pm 24\%$, and -5% to $+30\%$, respectively. The overbar denotes conventional time averaging.

The data acquisition system was a CAMAC (Computer Automated Measurement and Control) data acquisition system, controlled by a VAX 11/750. The CAMAC consisted of two LeCroy dual programmable amplifier with adjustable gain and offset, a LeCroy 8210 waveform analyzer that digitized up to four channels simultaneously at a maximum sampling rate of 1 MHz per channel, and three LeCroy 8800A memory modules. The maximum record length was 98304 words.

3. Mean flow results

The centreline floor pressure distribution is shown in figure 3. The pressure begins to rise at $x = 1.022$ m, reaches a peak at 1.273 m, and then decreases a little by $x = 1.324$ m before reaching its nominal downstream value. The region of variable pressure gradient extended approximately 11 times the incoming boundary-layer thickness, and in this distance the wall pressure increased by a factor of 1.9 ($\beta_{max} \equiv (\delta^*/\tau_w \partial p/\partial x)_{max} \approx 5.8$, a reasonably high value), and the free-stream Mach number dropped from 2.9 to 2.5. As can be seen, the agreement with the pressure distribution on the curved-wall model of Taylor (1984) (Model II) was very good.

The two-dimensionality of the flow field was of special concern since the pressure gradient generator (the contoured surface model) spanned the entire width of the

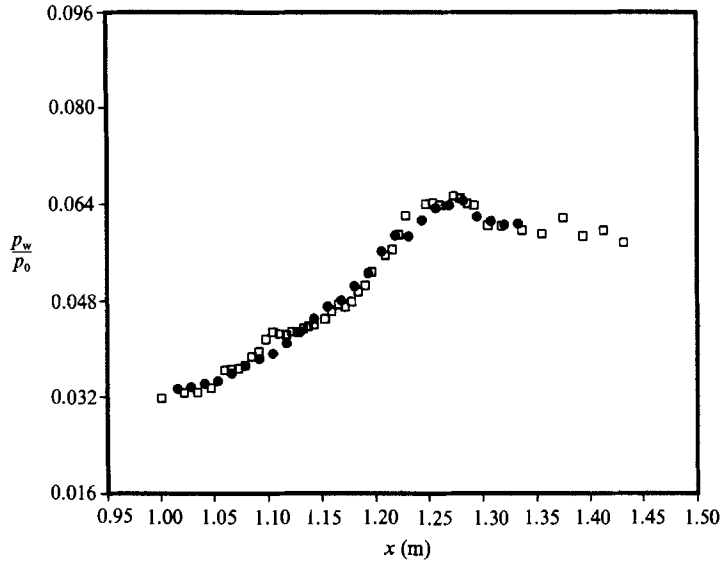

FIGURE 3. Wall static pressure distribution: □, current investigation; ●, Taylor (1984) Model II.

tunnel, thereby also imposing a pressure gradient on the sidewall boundary layers. Kerosene-lampblack surface-flow visualization showed that in the central portion of the flow field the surface-flow streaklines were parallel to the streamwise direction, whereas closer to the sidewalls the streaklines were directed slightly towards the tunnel centreline. Pitot pressure, static pressure and Preston probe surveys were made at 8 spanwise locations at $x = 1.324$ m. At this station, located downstream of the peak in the wall pressure, the skin-friction coefficient varied by less than $\pm 5\%$ over a spanwise distance of $4\delta_{\text{ref}}$ with no obvious periodicity. When compared to the measurements in the upstream boundary layer, there was no appreciable increase in the spanwise variations of the skin-friction coefficient owing to the imposed pressured gradient. Similarly, the spanwise variation of the surface pressure remained at about $\pm 3\%$ and showed no change through the region of changing pressure gradient.

However, the flow field measurements indicated that some degree of three-dimensionality occurred in the final stages of the pressure rise. At $x = 1.324$ m and 1.349 m, the stagnation pressure profiles for $0.0127\ m \leqslant z \leqslant 0.0472$ m showed a 'depression' near the boundary-layer edge ($z = 0$ is tunnel centreline). This systematic depression, with a maximum value of $0.1p_0$, where p_0 is the tunnel stagnation pressure, was probably due to a wave structure originating from the right tunnel wall, possibly from a poor joint between the tunnel sidewall and window. The effects of this wave structure were seen most strongly at $x = 1.324$ m, and it produced a variation of about $\pm 10\%$ in the various boundary-layer thicknesses over a spanwise distance of $4\delta_{\text{ref}}$.

Only four total temperature surveys were made within the pressure gradient region. Previous measurements in this facility, for a number of curved-wall flows and shock-wave/boundary-layer interactions (Taylor 1984; Settles 1975), showed that the total temperature profiles in the boundary layer did not vary significantly at any streamwise position. For the purpose of deriving the mean flow profiles, the total temperature variation over the boundary-layer thickness was approximated by a straight line with a slope of 4%. This approximation fitted the measured profiles of

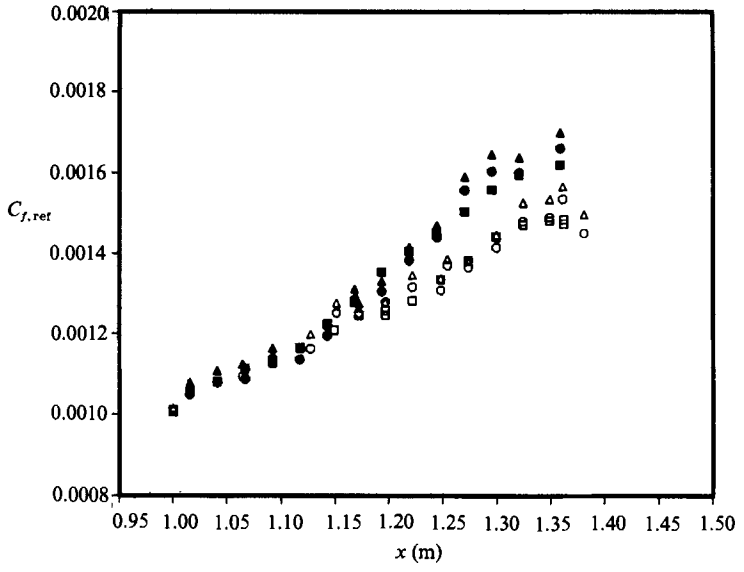

FIGURE 4. Streamwise variation of the skin friction for the present experiment (open symbols) and Taylor Model II (closed symbols). □, Preston probe, Bradshaw & Unsworth (1974*b*) calibration; ○, Clauser chart, Carvin *et al.* (1988) transformation; △, Clauser chart, Van Driest (1951) transformation.

T_t/T_0 to better than 1 %, where T_t is the local stagnation temperature and T_0 is the tunnel stagnation temperature.

The wall friction distributions were obtained by using a Preston probe, with the calibration suggested by Bradshaw & Unsworth (1974*b*), and the Clauser chart technique applied to the transformed velocity profile, where two different compressibility transformations were used, one by Van Driest (1951), and the other by Carvin, Debieve & Smits (1988). The transformation suggested by Carvin *et al.* does not assume the existence of a self-preserving boundary layer, although the actual differences between it and the van Driest transformation were found to be small.

The skin-friction coefficients, normalized by the upstream reference dynamic pressure, are shown in figure 4, together with the results obtained by Taylor for Model II. All three methods for determining $C_{f,\mathrm{ref}}$ agree to within 6% for each experiment. In Taylor's original presentation (see also Jayaram *et al.* 1987), the Preston probe results differed by up to 25% from the Clauser chart values. This discrepancy was due to the choice of two different edge conditions for the Preston probe and Clauser chart methods (see also Fernholz *et al.* 1988, Chap. 10). By using the upstream reference conditions, the skin-friction coefficients are not 'contaminated' by a poor choice of the boundary-layer edge state, which is particularly important in the region of pressure gradient.

On the flat plate, the wall friction reached a maximum at a point downstream of the wall pressure peak, before relaxing somewhat by the last measurement station. The behaviour is in contrast to that of an incompressible boundary layer where the wall friction decreases in response to an adverse pressure gradient. However, the behaviour of the friction velocity $u_\tau = (\tau_w/\rho_w)^{\frac{1}{2}}$ is more like that seen in an incompressible flow, in that u_τ fell to a minimum (at $x = 1.248$ m) before rising

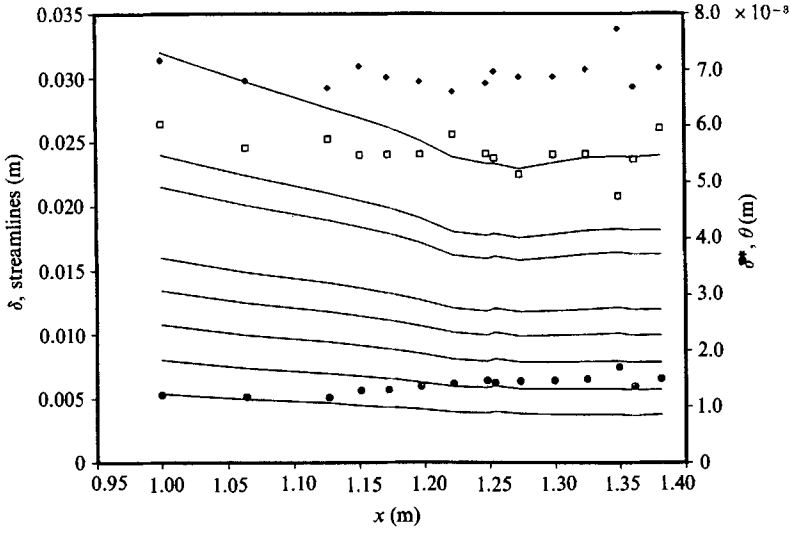

FIGURE 5. Selected mean streamlines, and streamwise variation of boundary-layer lengthscales along tunnel centreline. □, δ; ⊕, δ^*; ⊕, θ.

slightly and then remaining at essentially the same level till the last measurement station.

To plot $C_{f,\mathrm{ref}}$ for Model II in figure 4, Taylor's data points were shifted along the abscissa till the pressure distributions for the two experiments coincided. The physical locations of the upstream profiles differ by 124 mm. However, the differences seen in the upstream $C_{f,\mathrm{ref}}$ values for the two experiments reflects the streamwise variation in the undisturbed boundary layer due to the pressure of weak spurious wave systems, not the variation in Reynolds number. As in the current experiment, the wall friction in Model II increases in response to the perturbation. However, the peak amplification is about 17% larger than on the flat plate.

The streamwise variations of the boundary-layer thickness δ, displacement thickness δ^*, and momentum thickness θ are shown in figure 5. The boundary-layer thickness decreases initially, unlike its expected behaviour in an incompressible boundary layer. However, even though the boundary-layer thickness is decreasing, there is still entrainment of fluid into the boundary layer, as can be seen from the streamlines shown in the same figure. Additionally, the momentum thickness continues to increase within the adverse pressure gradient region. The same trends were observed by Taylor for Model II.

The streamwise velocity profiles, transformed according to Carvin *et al.* are shown in figure 6. The velocity profiles display a logarithmic region at all stations. However, towards the latter part of the pressure rise, the velocity profiles develop a 'dip' below the log law. This dip has been interpreted as indicating that the increase of the turbulence lengthscale with y is greater than that observed in equilibrium layers (Smits, Young & Bradshaw 1979). The dip first becomes noticeable at $x = 1.299$ m, that is, downstream of the point where the wall pressure reached its peak value, demonstrating the relatively slow response of the boundary layer to the adverse pressure gradient.

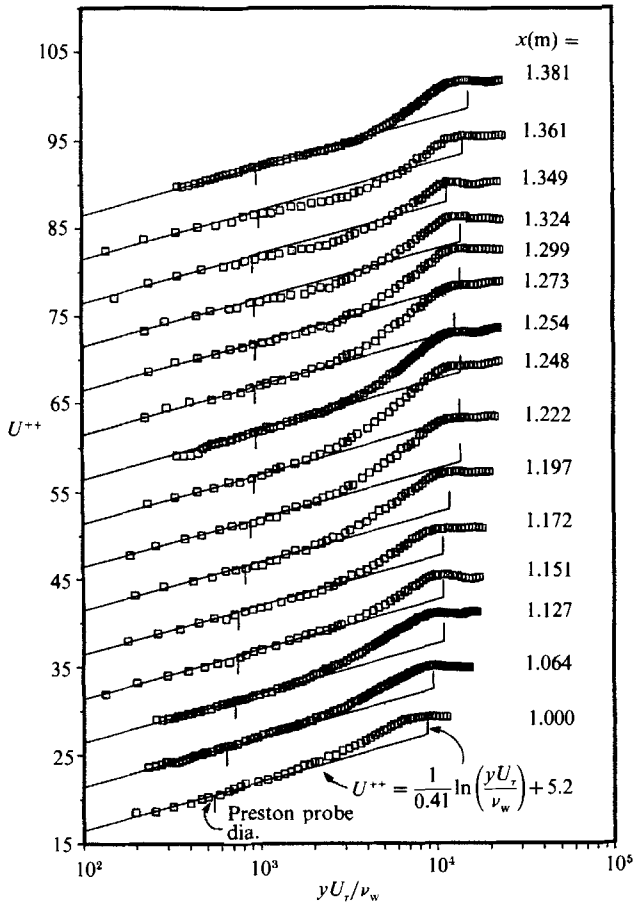

FIGURE 6. Tunnel centreline velocity profiles, transformed according to Carvin *et al.* (1988). Succeeding profiles have been shifted upwards by five units for clarity.

4. Turbulence results

The amplification of $(\overline{\rho u})'^2)^{\frac{1}{2}}/\overline{\rho U}$ (the quantity actually measured by a normal hot wire) was very small, and within the pressure gradient region the maximum amplification in the middle of the boundary layer was about 10%. However, since the mean mass flux in the free stream increased by a factor of 1.46 owing to the pressure rise, the increase in the absolute fluctuation level was considerable.

The Reynolds stresses $\overline{\rho u'^2}$, $\overline{\rho v'^2}$, and $-\overline{\rho u'v'}$, together with the kinematic quantities $\overline{u'^2}$, $\overline{v'^2}$, and $-\overline{u'v'}$, are shown in figures 7, 8 and 9 (the contributions to the Reynolds stresses from terms involving density fluctuations are an order of magnitude smaller and can be neglected). The profiles were scaled using several normalizations, including local mean values, local boundary-layer edge values, and upstream boundary-layer edge values. None of these normalizations succeeded in collapsing the stress profiles, and hence the upstream boundary-layer edge values were used to normalize the stress profiles presented here, and the profiles show the absolute variations in the stress levels.

As can be seen in figure 7, the amplification of $\overline{\rho u'^2}$ and $\overline{u'^2}$ were very similar, with a peak amplification factor in $\overline{\rho u'^2}$ of 2.8. The last profile shown displays some relaxation in the stress near the wall. The Reynolds shear stress $-\overline{\rho u'v'}$ was also

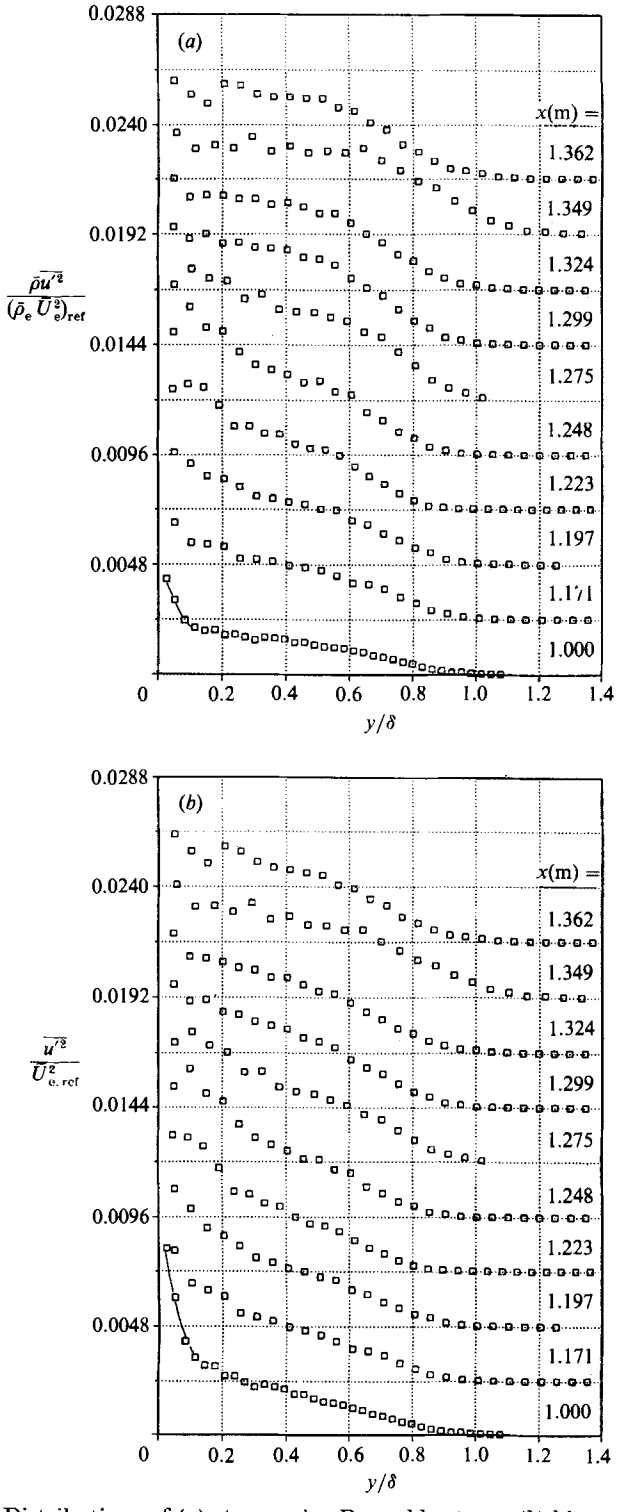

FIGURE 7. Distributions of (*a*) streamwise Reynolds stress, (*b*) kinematic turbulent intensity.

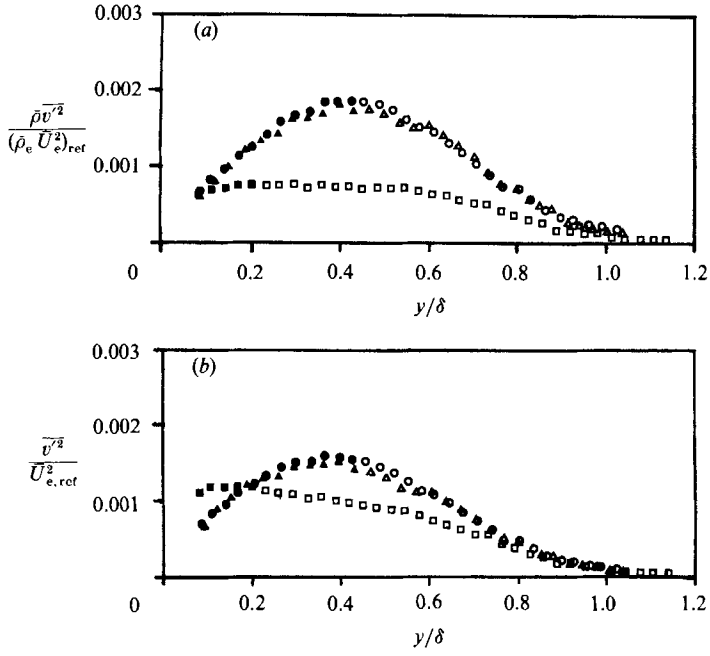

FIGURE 8. Distributions of (*a*) normal Reynolds stress, (*b*) kinematic turbulent intensity. □, x = 1.000 m; △, 1.254 m; ○, 1.381 m. Solid symbols indicate regions where crossed-wire results must be treated with caution.

amplified by a factor of about 2.5 (figure 9), and a strong maximum appeared in the mid-region of the layer. The wall friction matches well with the crossed-wire results in the upstream boundary layer, but further downstream the inaccuracies of the crossed-wire technique in the region near the wall are more apparent. The normal stress $\overline{\rho v'^2}$ (figure 8*a*) closely followed the behaviour of the shear stress, and the kinematic stresses all behaved similarly to the corresponding Reynolds stresses.

The variation of 'structure' parameters, such as the correlation coefficient $R_{uv} = -\overline{u'v'}/[(\overline{u'^2})^{\frac{1}{2}}(\overline{v'^2})^{\frac{1}{2}}]$, the anisotropy ratio $\overline{u'^2}/\overline{v'^2}$, and $a_1' \equiv -\overline{u'v'}/q^2$, where it was assumed that $q^2 = 1.5(\overline{u'^2}+\overline{v'^2})$, are shown in figure 10. It can be seen that they display much less variation than the stresses themselves. For example, the anisotropy ratio has an average value of about 2.2 at all three measurement stations. The correlation coefficient between u' and v' decreases away from the wall in the upstream boundary layer, with an average value of approximately 0.3. Within the perturbation region R_{uv} increases by approximately 25% across most of the boundary layer, implying that the pressure gradient preferentially amplifies the shear stress over the normal stresses. This can also be seen in the behaviour of a_1': in the upstream boundary layer this ratio decreases away from the wall and has an average value of about 0.11 in the lower half of the layer, and in response to the pressure gradient this value increases to about 0.15.

When these stress ratios are compared to results obtained in incompressible boundary layers some interesting differences are observed. For example, the ratio $-\overline{u'v'}/q^2 = a_1$ has a constant value of ≈ 0.15 in zero pressure gradient subsonic boundary layers (Bradshaw 1967) whereas the upstream boundary layer in the present case shows a continual decrease from about 0.15 near the wall to about 0.08 at the boundary-layer edge. The shear correlation coefficient R_{uv} also decreases

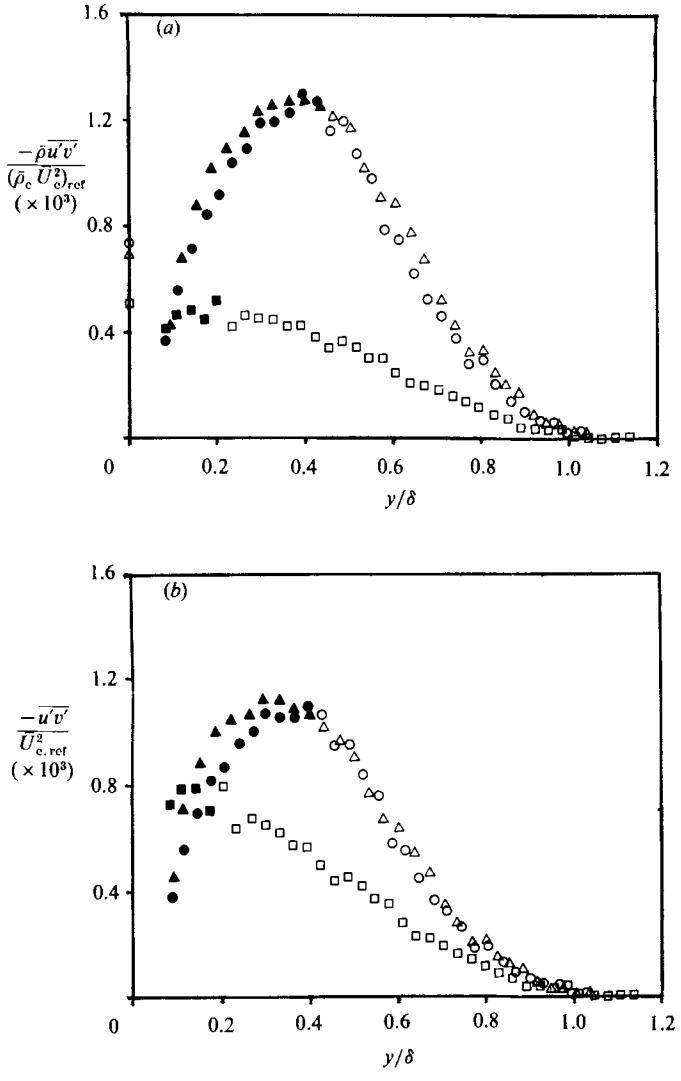

FIGURE 9. Distributions of (*a*) Reynolds shear stress, (*b*) kinematic shear stress. □, $x = 1.000$ m; △, 1.254 m; ○, 1.381 m. Wall values obtained from measurements of skin friction. Solid symbols indicate regions where crossed-wire results must be treated with caution.

as y/δ increases, whereas in subsonic flow it has a nearly constant value of 0.45 for $0 < y/\delta < 0.8$ (Alving 1988). Finally, the anisotropy ratio is about 40% higher than the value seen in subsonic flows.

Despite the uncertainties associated with crossed-wire measurements in supersonic flow, the differences observed between compressible and incompressible zero pressure gradient flows are probably real, since the differences are most obvious in the middle of the boundary layer where the crossed-wire technique has the least uncertainty. In fact, the systematic error introduced by the use of the Strong Reynolds Analogy implies that the value of R_{uv} is *overestimated* by up to 20%. The recent calculations by Dussauge & Quine (1988) suggest that compressibility reduces R_{uv} to levels which agree well with our best estimate of the experimental values. Furthermore, in an incompressible boundary layer a_1 decreases in response to an adverse pressure

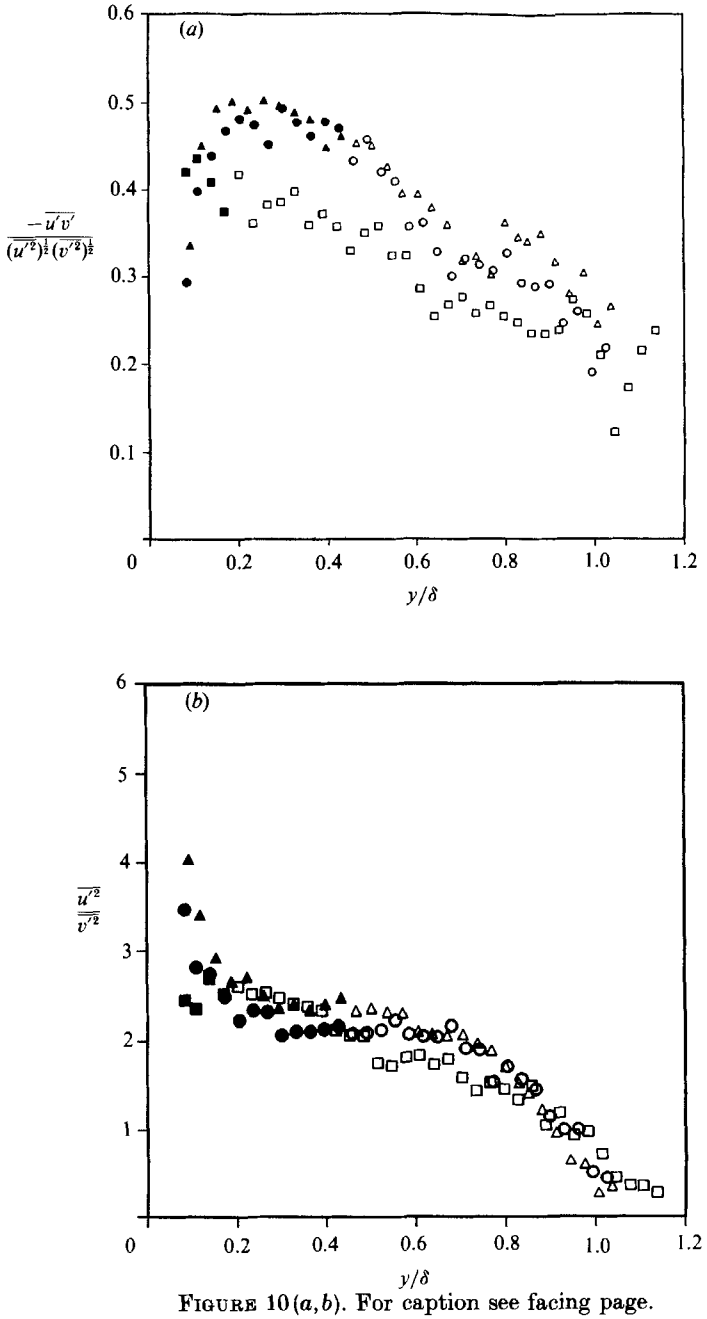

FIGURE 10(*a*,*b*). For caption see facing page.

gradient ($\beta = 5.4$, Bradshaw 1967), whereas in the present case it increases. It seems that the structure parameters also depend on the nature and strength of the perturbation (Jayaram *et al.* 1987). For example, Ardonceau (1984) observed an increase in the anisotropy ratio for a shock-wave/boundary-layer interaction, whereas this ratio remains unchanged in the present experiment.

To further investigate the response, figure 11 shows the amplification of $\overline{\rho u'^2}$ along streamlines originating at various points in the upstream boundary layer. The

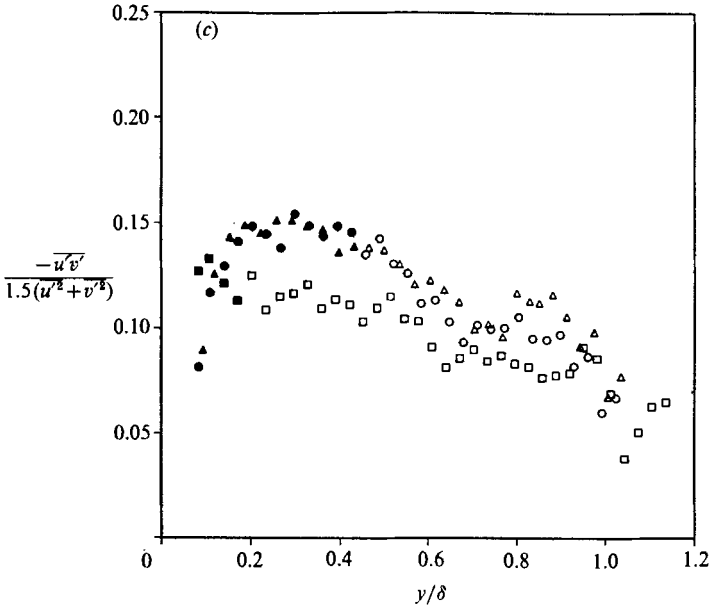

FIGURE 10. Distributions of structure parameters (*a*) Correlation coefficient between u' and v', (*b*) anisotropy parameter, (*c*) ratio of shear stress to turbulent kinetic energy. □, $x = 1.000$ m; △, $x = 1.254$ m; ○, $x = 1.381$ m. Solid symbols indicate regions where crossed-wire results must be treated with caution.

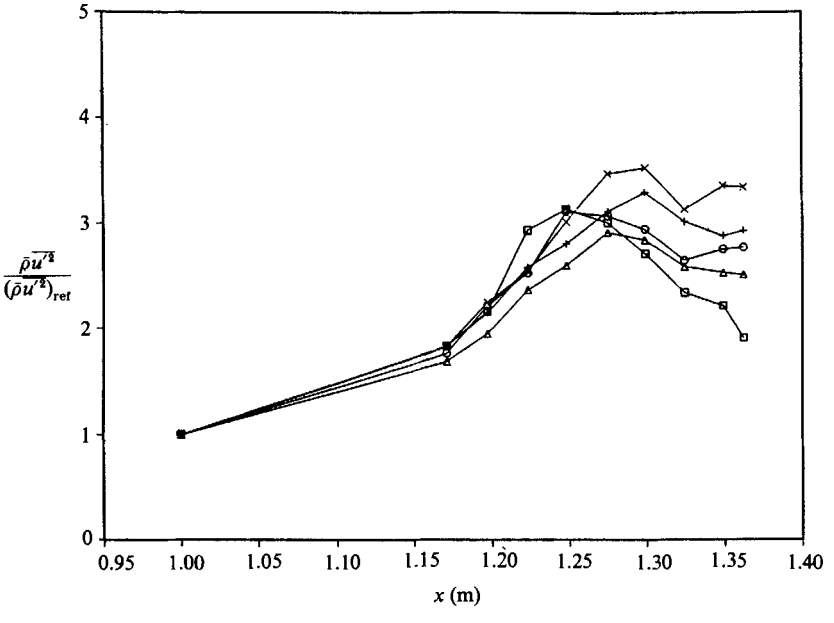

FIGURE 11. Evolution of streamwise Reynolds stress along streamlines originating at various points in the upstream boundary layer: □, $y/\delta = 0.2$; ○, 0.3; △, 0.4; +, 0.5; ×, 0.6.

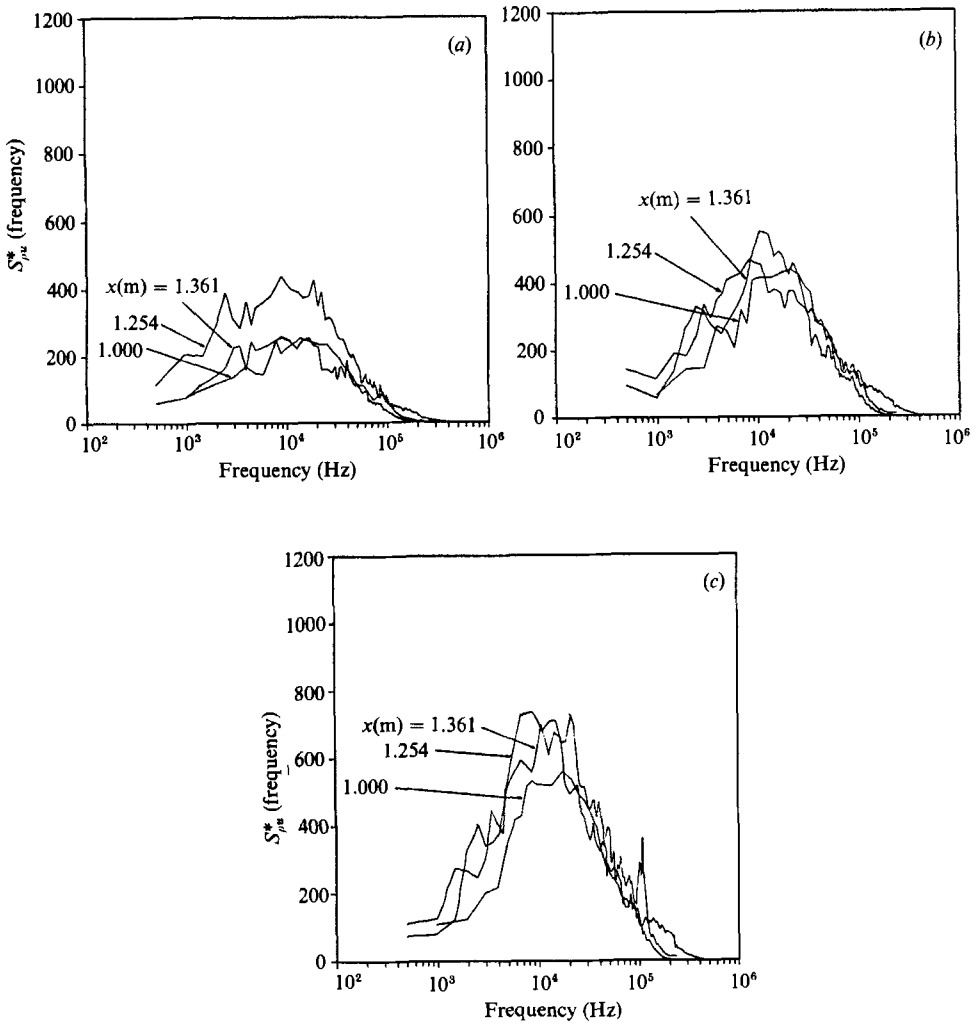

FIGURE 12. Evolution of the $(\rho u)'$ spectrum along three streamlines originating at (*a*) $y/\delta = 0.2$, (*b*) 0.4, (*c*) 0.6.

maximum amplification is approximately the same along all streamlines shown, and the y-dependence only becomes apparent downstream of the peak in the wall pressure. In contrast, the behaviour $\overline{\rho v'^2}$ and $-\overline{\rho u'v'}$ along streamlines (not shown) is more dependent on streamline position in the boundary layer, where the amplification is considerably greater along the outer layer streamlines. Not unexpectedly, all three turbulent stresses show a faster relaxation near the wall.

The energy spectra of the fluctuating mass flux at points along three particular streamlines are plotted in figure 12. The spectra are shown so that the area under each curve represents the mean square value of the signal and the peak corresponds to the frequency of the most energetic motions ($f_{\max}$). The amplification and consequent relaxation of the turbulence level is clearly observed. Note that along the two streamlines closest to the wall, $f_{\max}$ decreases within the pressure gradient flow. This decrease was also observed on the curved-wall models studied by Jayaram *et al.* (1987), (including Model II of Taylor) and by Smits & Muck (1987) in shock-

wave/boundary-layer interactions. This decrease in f_{max} implies an increase in the near-wall lengthscale over its equilibrium value, which is consistent with the observed dip in the log-law profiles. It is interesting to note that the effects of an increased lengthscale are seen first in the spectra (at $x = 1.248$ m) and only later in the form of a dip below the log law (at $x = 1.299$ m), suggesting that the logarithmic velocity profile is less sensitive to departures from equilibrium than the spectra.

5. Correlation measurements

Dual normal hot wires were used to measure space–time correlations between mass-flux signals in the spanwise and vertical directions. It was found that the correlation coefficient $R_{\rho u}$ had a well-defined maximum at a time delay τ_{max}, and the maximum value of $R_{\rho u}$ and τ_{max} depended on the wire spacing.

The peak values of the correlation coefficients for wires separated in the vertical direction are shown in figure 13. The correlation coefficients for large time delays were typically 0.1, much smaller than the peak values, which suggests that the effect of systematic errors on the peak correlation coefficients was small. As expected, the peak value is lower for the wires with larger separation, at all heights. The maximum value of the peak cross-correlation coefficient occurs in the mid-region of the layer, suggesting that the organized motions are most coherent there. For the wires with small separation ($0.09\delta_{ref}$), the peak value of $R_{\rho u}$ drops within the pressure gradient flow, most noticeably in the outer parts of the layer. However, by the furthest downstream station, it has nearly recovered to its upstream value. The results for the wires with larger separation ($0.18\delta_{ref}$) are much the same, except that the drop in the correlation coefficient is more pronounced across the whole layer. It appears that the vertical extent of the organized motions is reduced by the adverse pressure gradient, but that it recovers quickly. Furthermore, the relatively high correlation coefficient for a vertical separation distance of $0.18\delta_{ref}$ suggests that these structures maintain their identity over a large fraction of the layer. This is consistent with the suggestion by Spina & Smits (1987) that the largest structures have a height comparable with the boundary-layer thickness.

The behaviour of the peak cross-correlation coefficient for wires separated in the spanwise direction (figure 14) is slightly different. First, the maximum level occurs further out in the layer, and there is no decrease across the pressure gradient region. Second, the peak coefficients for the spanwise separated wires are slightly lower than those for the vertically separated wires, indicating that the vertical and spanwise extent of these structures are different, and that they are affected differently by the pressure gradient. However, the spanwise correlation over distances of $0.18\delta_{ref}$ are still significant. Now, Spina & Smits used wall-pressure/mass-flux correlations to conclude that the large-scale motions are of limited spanwise extent, and of the order of $0.1\delta_{ref}$. Their conclusion is probably misleading for two reasons. First, the correlation coefficient between the spanwise separated wires decreases near the wall, indicating that the organized structures are of smaller spanwise extent near the wall. Hence for a given spanwise separation between probes, and with the hot wire(s) at a fixed distance away from the wall, wall-pressure/mass-flux correlations will be lower than the mass-flux cross-correlations between hot wires. Secondly, the lower values of the peak cross-correlation for vertically separated wires in the region near the wall (figure 13) indicate that the structures become less coherent closer to the wall, and therefore wall-pressure/hot-wire mass-flux correlations must be lower than mass-flux/mass-flux correlations. Thus it seems that the structures have a larger

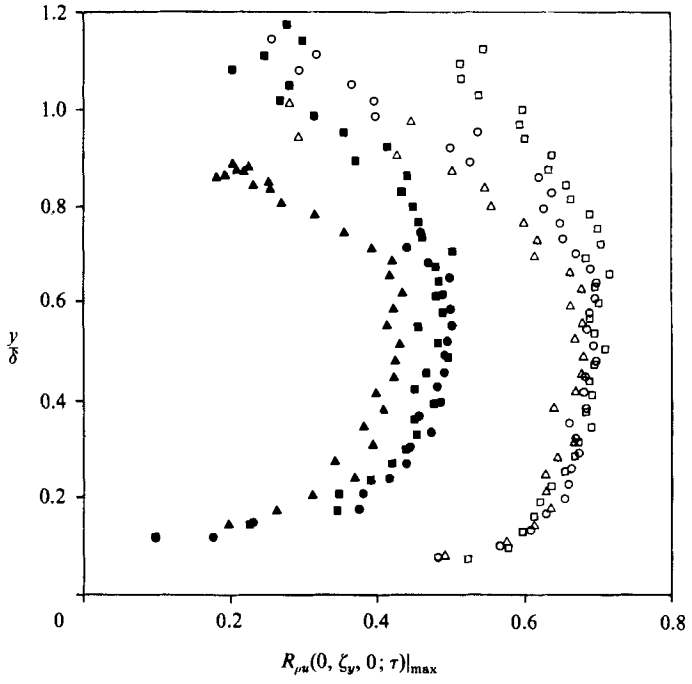

FIGURE 13. Variation of the peak mass-flux cross-correlation between vertically separated hot wires. □, $x = 1.000$ m; △, 1.254 m; ○, 1.381 m. Open symbols $\xi = 0.09$, closed symbols $\xi = 0.18$.

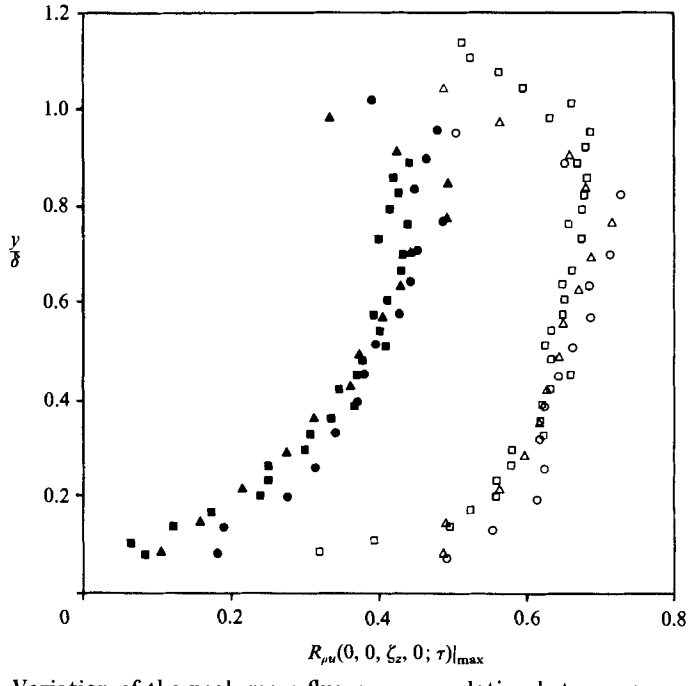

FIGURE 14. Variation of the peak mass-flux cross-correlation between spanwise separated hot wires. Symbols as in figure 13.

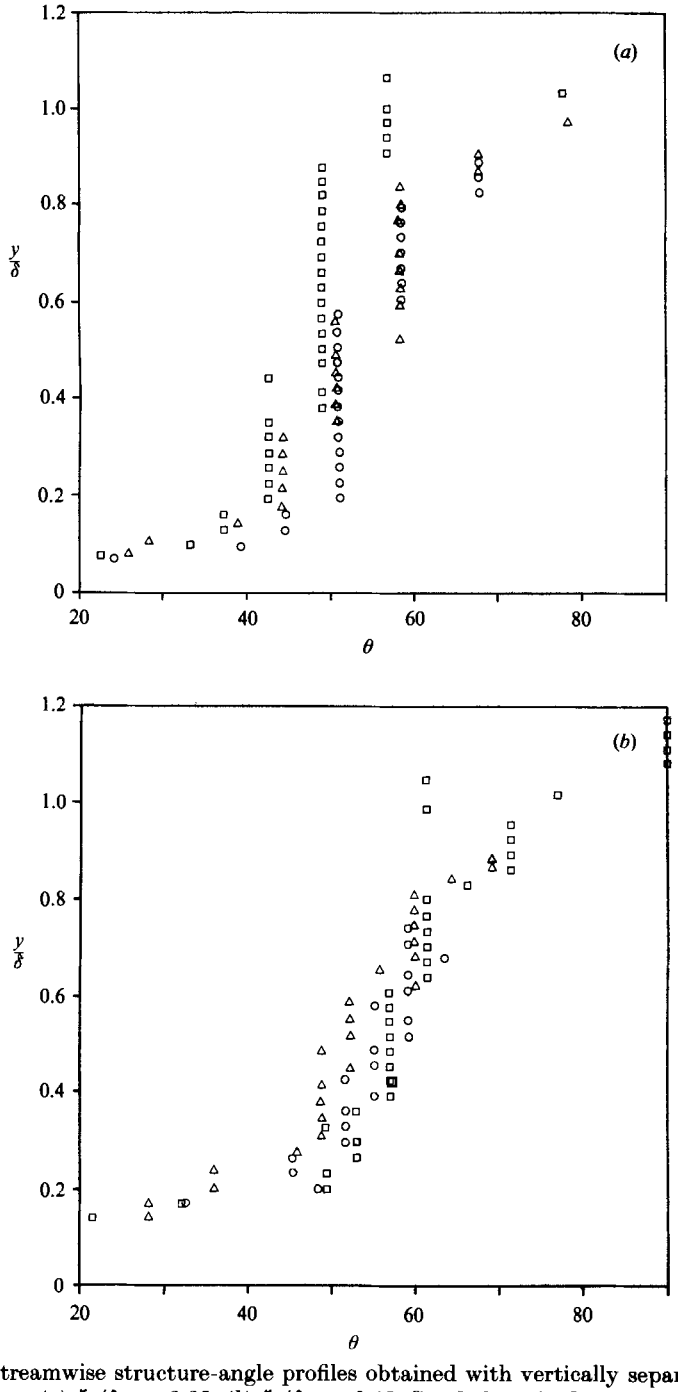

FIGURE 15. Streamwise structure-angle profiles obtained with vertically separated hot wires: (*a*) $\xi_y/\delta_{\text{ref}} = 0.09$, (*b*) $\xi_y/\delta_{\text{ref}} = 0.18$. Symbols as in figure 13.

spanwise extent than suggested by Spina & Smits. Furthermore when these correlation coefficients are compared to those obtained by Alving (1988) in a subsonic zero pressure gradient layer for the same vertical wire separations ξ_y/δ, it was seen that the cross-correlation coefficient is higher in supersonic flow. Similarly, Favre's (1965) subsonic results show that equivalent correlation coefficients are higher in supersonic flow.

The time delay corresponding to the maximum in the correlation, $\tau_{\max}$, may be interpreted in terms of a 'structure angle' θ, first defined by Spina & Smits (1987) as

$$\theta = \arctan\left(\frac{\xi_y}{U_c T_{\max} + \xi_x}\right), \tag{2}$$

where ξ_x is the small streamwise misalignment between the two vertically separated hot wires ($\xi_x < \xi_y/10$). Recent measurements by Spina (1988) in the upstream boundary layer showed that the convection velocity U_c was about $0.9U$ across most of the layer. High-speed schlieren cine-film obtained in the same flow by Smith & Smits (1988) also showed the convection velocity of density gradient structures to be about $0.9U$. A constant value of $0.9U$ was therefore assumed in calculating θ, and it was not directly measured. It should be noted that the sensitivity of the structure angle to any uncertainty in the convection velocity is small. For example, a 10% error in U_c changes θ by a maximum of only 3°.

The structure angles obtained using two different wire spacings are shown in figure 15. From the results with small separation ($0.09\delta_{\text{ref}}$), it can be seen that in the incoming boundary layer the structure angle was approximately 50° over the middle portion of the layer, with a decrease in angle near the wall and an increase near the boundary-layer edge. The structure angle also increases a little through the pressure gradient region. However, the observed increase is at the limits of the experimental resolution (±4°) and this result must be treated as inconclusive, especially since the results from the wires with large separation ($0.18\delta_{\text{ref}}$) are different in two aspects: the inferred structure angle is larger, being approximately 57° rather than 50° in the middle of the layer, and the structure angle shows no change across the pressure gradient region. A similar variation of the structure angle with wire spacing was also observed by Alving (1988) and Spina (1988), and the results would seem to indicate that the larger structures have a larger angle of inclination to the wall. It seems unlikely that changes in the convection velocity for different scale structures are responsible because of the large change required (approximately 29%).

It is widely believed that the large-scale structure angle and the angle of inclination of the principal axis with pure stretching strain should be the same. In the present experiment the angle of the inclination of the principal axis decreases by approximately 5° as the flow passes through the region of pressure gradient, but the structure angle shows no such decrease. However, more experiments with better resolution of structure angles and larger charges in the principal axis angle are required before any definite link between the two can be established.

6. Discussion

In comparing the present results to those of Taylor, the total impulse in extra strain rate, defined as $I = \int e\,dt$, where e is the applied extra strain rate, can be used as a rough measure. For longitudinal streamline curvature $e = \partial V/\partial x$, and for dilatation $e = \nabla \cdot U$. For an impulse in dilatation, we obtain $I = (1/\gamma)\log(p_2/p_1)$, where p_2/p_1 is the static pressure rise (Hayakawa, Smits & Bogdonoff 1984).

Similarly, for an impulse in curvature, $I = \beta$, where β is the total turning angle (Smits *et al.* 1979). When the extra strain rates are applied over a distance comparable with the response lengthscale of the large eddies in the boundary layer ($\approx 10\delta$), as in the present case, the perturbations are no longer true impulses. However, the impulse value can still be used to make some crude comparisons among different experiments.

In Taylor's experiment the adverse pressure gradient was primarily due to longitudinal streamline curvature, with a total turning angle of 8°. In the present investigation, the adverse pressure gradient was imposed externally, and the maximum turning angle was less than 3°, near the boundary-layer edge at $x = 1.222$ m. Because the pressure rise was the same in the two experiments, the impulse due to dilatation was also the same, and equal to 0.46. In Taylor's experiment the additional impulse due to turning was 0.14, one third the impulse due to dilatation.

The mean flow and turbulence behaviour in the curved-wall and flat-plate experiments was qualitatively similar. The similarity in behaviour of the boundary-layer lengthscales for the two tests has already been mentioned in §3. In both experiments the velocity profiles displayed a dip below the log law, and in this region the frequency of the most energetic motions decreased. In addition, the large-scale structure angle shows no change across the perturbation in the present test and in the curved-wall flow (Donovan & Smits 1987). Donovan & Smits suggested that in the curved-wall flow the perturbation rate may be slow enough to allow the large-scale motions to readjust to the new boundary conditions and thus maintain their angle of inclination. For instance, the VITA ensemble-averaged $(\rho u)'$ signatures showed an increase in amplitude through the curved region. However, when normalized by the local r.m.s. values, the ensemble averages remained essentially the same across the perturbation. The behaviour of the VITA ensemble averages in the current experiment (results not shown) was similar to that observed in the curved-wall study, and it seems that the large-scale structures in both experiments show only small changes in their identity due to the perturbation.

However, even though the overall behaviour may be qualitatively similar, the details were significantly different. For example, the velocity profiles for the curved-wall model (see Jayaram *et al.* 1987) developed a dip below the log law sooner, and it persisted for a longer duration; the dip was first observed 0.127 m after the beginning of curvature, and it persisted up to the last measurement station. In the present test the dip was first observed 0.277 m into the pressure rise and it had disappeared by $x = 1.381$ m. At the point where the dip was first seen, the impulse in extra strain rate experienced by the boundary layer in the curved-wall case was 0.1 due to streamline curvature and 0.26 due to bulk compression, whereas the corresponding value in the flat-plate experiment was 0.47 (due to bulk compression). Thus it is seen that either the effects of concave curvature and bulk compression combine strongly, or that concave curvature has a much larger effect than bulk compression on the velocity profiles.

In the curved-wall case, the longitudinal Reynolds stress profile showed a peak amplification of 4.4 at a location 229 mm downstream of the start of curvature, while the shear stress showed a peak amplification of 3.3 at this location. The corresponding maximum amplification factors in the present investigation were 2.8 for the longitudinal stress at a location 226 mm into the pressure rise, and 2.5 for the shear stress at a location 232 mm into the pressure rise. Hence, the additional effect of curvature is more pronounced on the normal stress, although it has a significant effect on the shear stress as well.

The effect of curvature on the wall friction was not so pronounced. For the curved-

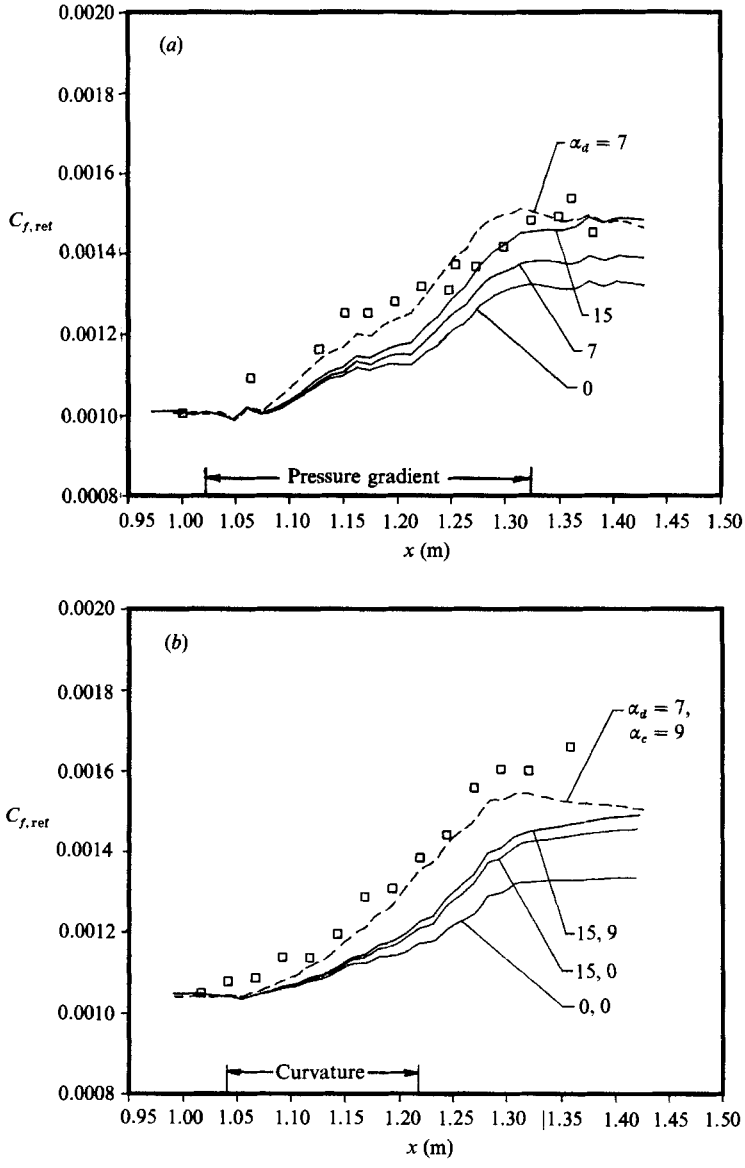

FIGURE 16. Comparison between measured and computed skin-friction variation for (*a*) flat-plate experiment, (*b*) Model II experiment. □, experiment (Preston probe); ——, computation, with lag; ---, computation, no lag. Note that $\frac{1}{2}\rho_e U_e^2$ increases by a factor of 1.34 from $x = 1.000$ m to $x = 1.381$ m in (*a*) and by a factor of 1.31 from $x = 1.016$ m to $x = 1.358$ m.

wall experiment the increase in the wall friction was only approximately 17% larger than in the flat-plate case, and it seems that the combined effects of curvature and bulk compression on the wall friction is a little smaller than that suggested by the linear addition of the impulse strengths (0.46+0.14).

To further identify the effects of the extra strain rates the wall stress distributions for the flat-plate case and the curved-wall model were computed using the 'one equation' method of Bradshaw & Unsworth (1974*a*). In that method, the model equation for the Reynolds stress was derived by simplifying the turbulent kinetic

energy equation, and since the effects of extra strain rates were found to be an order of magnitude larger than given by this equation, an empirical correction was applied to the model dissipation term (Bradshaw 1974). That is, the dissipation lengthscale was multiplied by a factor F that depends on the relative strength of the extra strain rate, where

$$F = 1 + \alpha \frac{e}{\partial U/\partial y}, \tag{3}$$

where α is a constant of $O(10)$. Note that the computation accounts for curvature ($\alpha = \alpha_c$) by a similar F-factor in the turbulence model equation as for bulk compression ($\alpha = \alpha_d$), and therefore assumes that combinations of extra strain rates can be linearly summed (Bradshaw & Ferriss 1971). Additionally, the model assumes that the structure parameter a_1, is a constant ($= 0.15$). The Bradshaw & Unsworth method was chosen to determine the performance of a simple calculation method in this relatively complex flow, and to determine the typical magnitude of empirical extra-strain rate corrections.

The results for the flat-plate experiment using different values of α are shown in figure 16(*a*). It can be seen that with $\alpha_d = 0$ (no correction for bulk compression effects), the computation underpredicts the skin friction, and that the final downstream value is low by about 11%. It seems that bulk compression has a significant effect on the skin friction variation, and by setting $\alpha_d = 15$ reasonable agreement was obtained between measured and computed values. However, within the initial part of the pressure gradient, the computation still underpredicted the skin friction, owing in part to the lag equation used by Bradshaw (1974) to account for the history of the extra strain rate. When the lag in the response was removed, and α_d was set to 7, as suggested by Bradshaw for bulk compression, the agreement with experiment was much improved. Bulk compression seems to act immediately, and a lagged response does not seem to be necessary.

For the curved-wall case, the influence of bulk compression was examined by setting $\alpha_d = 0$ and $\alpha_d = 15$ in the computation, and the influence of streamwise curvature was examined by setting $\alpha_c = 0$ and $\alpha_c = 9$ (the value suggested by Bradshaw). It can be seen from figure 16(*b*) that with the bulk compression and wall curvature corrections 'on', the lagged computation is unable to match the experimental values, but when the lag in the response was removed, $\alpha_d = 7$ and $\alpha_c = 9$ gave a very good match with experiment.

7. Conclusions

Despite the large increases observed in the Reynolds stress components, the effect of the adverse pressure gradient on the flat-plate turbulence structure is relatively mild; the ratios of the stresses, and the general features of the space–time correlations appear to be virtually unaltered. The strongest feature of the boundary-layer response appears to be an increase in the lengthscale, leading to a dip in the logarithmic velocity profiles and a shift towards lower frequencies in the spectra. For the flow on a curved wall with the same pressure distribution, the most significant differences are seen in the absolute stress behaviour. The disturbances experienced in both the curved-wall and the flat-plate flows appear to lie within the scope of current prediction methods, and the empirical modifications suggested by Bradshaw for the effects of compression seem to describe the skin-friction behaviour quite well, although compression effects appear to act immediately with no lag in the response.

This work was supported by AFOSR Grants 85-0126 and 88-0120 monitored by Dr James McMichael.

REFERENCES

ALVING, A. A. 1988 Boundary layer relaxation from curvature. Ph.D. thesis, Mechanical and Aerospace Engineering Department, Princeton University.

ARDONCEAU, P. L. 1984 The structure of turbulence in a supersonic shock wave/boundary layer interaction. *AIAA J.* **22**, 1254–1262.

BRADSHAW, P. 1967 Irrotational fluctuations near a turbulent boundary layer. *J. Fluid Mech.* **27**, 209–230.

BRADSHAW, P. 1973 The effect of streamline curvature on turbulent flow. AGARDograph 169. NATO.

BRADSHAW, P. 1974 The effect of mean compression or dilatation on the turbulence structure of supersonic boundary layers. *J. Fluid Mech.* **63**, 449–464.

BRADSHAW, P. & FERRISS, D. H. 1971 Calculation of boundary-layer development using the turbulent energy equation: compressible flow on adiabatic walls. *J. Fluid Mech.* **46**, 83–110.

BRADSHAW, P. & UNSWORTH, K. 1974 *a* An improved FORTRAN program for the Bradshaw-Ferriss-Atwell method of calculating turbulent shear layers. *Aero Rep.* 74-02. Imperial College, London.

BRADSHAW, P. & UNSWORTH, K. 1974 *b* Comment on 'Evaluation of Preston tube calibration equations in supersonic flow'. *AIAA J.* **12**, 1293–1295.

CARVIN, C., DEBIEVE, J. F. & SMITS, A. J. 1988 The near wall temperature profile of turbulent boundary layers. *AIAA Paper* 88-0136.

DONOVAN, J. F. & SMITS, A. J. 1987 A preliminary investigation of large-scale organized motions in a supersonic turbulent boundary layer on a curved surface. *AIAA Paper* 87-1285.

DUSSAUGE, J.-P. & QUINE, C. 1988 A second-order closure for supersonic turbulent flows. Application to the supersonic mixing. *Symp. on The Physics of Compressible Turbulent Mixing, Princeton University, Princeton, N.J.* Springer (to be published).

FAVRE, A. J. 1965 Review on space–time correlations in turbulent fluids. *Trans. ASME* E: *J. Appl. Mech.* **32**, 261.

FERNANDO, E. M. 1988 Supersonic turbulent boundary layer in an adverse pressure gradient. Ph.D. thesis, Mechanical and Aerospace Engineering Department, Princeton University.

FERNANDO, E. M., DONOVAN, J. F. & SMITS, A. J. 1987 The calibration and operation of a constant temperature cross-wire probe in supersonic flow. *Symp. of Thermal Anemometry, Cincinnati, Ohio.* ASME.

FERNHOLZ, H. H., SMITS, A. J., DUSSAUGE, J. P. & FINLEY, P. J. 1988 A survey of measurements and measuring techniques in rapidly distorted compressible turbulent boundary layers. *NATO Advisory Group for Aerospace Research and Development, AGARDograph* 315.

HAYAKAWA, K., SMITS, A. J. & BOGDONOFF, S. M. 1984 Turbulence measurements in a compressible reattaching shear layer. *AIAA J.* **22**, 889–895.

HOFFMAN, P. H., MUCK, K. C. & BRADSHAW, P. 1985 The effect of concave surface curvature on turbulent boundary layers. *J. Fluid Mech.* **161**, 371–403.

JAYARAM, M., TAYLOR, M. W. & SMITS, A. J. 1987 The response of a compressible turbulent boundary layer to short regions of concave surface curvature. *J. Fluid Mech.* **175**, 343–362.

MORKOVIN, M. V. 1961 Effects of compressibility on turbulent flows. In *Mecanique de la Turbulence* (ed. A. Favre). CNRS.

MUCK, K. C., HOFFMAN, P. H. & BRADSHAW, P. 1985 The effect of convex surface curvature on turbulent boundary layers. *J. Fluid Mech.* **161**, 347–369.

RAMAPRIAN, B. R. & SHIVAPRASAD, B. G. 1978 The structure of turbulent boundary layers along mildly curved surfaces. *J. Fluid Mech.* **85**, 273–303.

SETTLES, G. S. 1975 An experimental study of compressible turbulent boundary layer separation at high Reynolds numbers. Ph.D. thesis, Mechanical and Aerospace Engineering Department, Princeton University.

SMITH, M. W. & SMITS, A. J. 1988 A cinematic visualization of coherent density structures in a supersonic turbulent boundary layer. *AIAA Paper* 88-0500.

SMITS, A. J., HAYAKAWA, K. & MUCK, K. C. 1983 Constant temperature hot-wire practice in supersonic flows, Part I: The normal wire. *Exp Fluids* **1**, 83–92.

SMITS, A. J. & DUSSAUGE, J. P. 1988 A survey of measurements and measurement techniques in rapidly distorted compressible turbulent boundary layers. AGARDograph 315, Chapter 5 (see Fernholz *et al.* 1988).

SMITS, A. J., ALVING, A. E., SMITH, R. W., SPINA, E. F., FERNANDO, E. M. & DONOVAN, J. F. 1988 A comparison of the turbulence structure of subsonic and supersonic boundary layers. *Eleventh Symp. on Turbulence, University of Missouri-Rolla, October.* (See also *Phys. Fluids* A **1**, 1989, 1865–1875.)

SMITS, A. J. & JOUBERT, P. N. 1982 Turbulent boundary layers on bodies of revolution. *J. Ship Res.* **26**, 135–147.

SMITS, A. J. & MUCK, K. C. 1984 Constant temperature hot-wire anemometer practice in supersonic flows. Part II. The inclined wire. *Exps Fluid* **2**, 33–41.

SMITS, A. J. & MUCK, K. C. 1987 Experimental study of three shock wave/turbulent boundary layer interactions. *J. Fluid Mech.* **182**, 291–314.

SMITS, A. J., YOUNG, S. T. B. & BRADSHAW, P. 1979 The effect of short regions of high surface curvature on turbulent boundary layers. *J. Fluid Mech.* **94**, 209–242.

SPINA, E. F. 1988 Organized structures in a supersonic turbulent boundary layer. Ph.D. thesis, Mechanical and Aerospace Engineering Department, Princeton University.

SPINA, E. F. & SMITS, A. J. 1987 Organized structures in a compressible turbulent boundary layer. *J. Fluid Mech.* **182**, 85–109.

TAYLOR, M. W. 1984 A supersonic turbulent boundary layer on concavely curved surfaces. *Princeton University Mechanical and Aerospace Engng Rep.* 1684.

VAN DRIEST, E. R. 1951 Turbulent boundary layer in compressible fluids. *J. Aero. Sci.* **18**, 145–160 and 216.